

1 **Tailoring single-atom FeN₄ moieties as a robust heterogeneous**
2 **catalyst for high-performance electro-Fenton treatment of**
3 **organic pollutants**

4 Pan Xia ^a, Zhihong Ye ^{a,*}, Lele Zhao ^b, Qian Xue ^c, Sonia Lanzalaco ^d, Qiang
5 He ^a, Xueqiang Qi ^c, Ignasi Sirés ^{b,**}

6 ^a *Key Laboratory of Eco-environments in Three Gorges Reservoir Region, Ministry of*
7 *Education, College of Environment and Ecology, Chongqing University, Chongqing,*
8 *400045, China*

9 ^b *Laboratori d'Electroquímica dels Materials i del Medi Ambient, Departament de*
10 *Ciència de Materials i Química Física, Secció de Química Física, Facultat de Química,*
11 *Universitat de Barcelona, Martí i Franquès 1-11, 08028 Barcelona, Spain*

12 ^c *School of Chemistry & Chemical Engineering, Chongqing University of Technology,*
13 *Chongqing 400054, China*

14 ^d *Departament d'Enginyeria Química and Barcelona Research Center in Multiscale*
15 *Science and Engineering, EEBE, Universitat Politècnica de Catalunya, C/Eduard*
16 *Maristany, 10-14, 08019 Barcelona, Spain*

17 * Corresponding author: yezhihong@cqu.edu.cn (Z. Ye)

18 ** Corresponding author: i.sires@ub.edu (I. Sirés)

19 **Abstract**

20 An iron single-atom catalyst, composed of robust FeN₄ moieties anchored on a nitrogen-
21 doped porous carbon matrix (Fe-SAC/NC), has been developed via a surfactant-
22 coordinated metal-organic framework (MOF) approach for application in heterogeneous
23 electro-Fenton (HEF) process. The cohesive interaction between the surfactant and MOF
24 precursor enabled the formation of abundant and stable FeN₄ moieties. The Fe-SAC/NC-
25 catalyzed HEF allowed the complete degradation of 2,4-dichlorophenol with low iron
26 leaching (1.2 mg L⁻¹), being superior to nanoparticle catalyst synthesized without
27 surfactant. The experiments and density functional theory (DFT) calculations
28 demonstrated the dominant role of single-atom FeN₄ sites to activate the electrogenerated
29 H₂O₂ yielding •OH. The dense FeN₄ moieties allowed harnessing the modulated
30 electronic structure of the SAC to facilitate the electron transfer, whereas the adjacent
31 pyrrolic N enhanced the adsorption of target organic pollutants. Moreover, the excellent
32 catalysis, recyclability and viability of the Fe-SAC/NC were verified by treating several
33 organic pollutants even in urban wastewater.

34 **Keywords:** Advanced oxidation process; Electro-Fenton; Metal-organic framework;
35 Single-atom catalyst; Water treatment

36

37 **1. Introduction**

38 As a result of the booming demand of healthcare products (e.g., pharmaceuticals),
39 crop protection products (e.g., pesticides) and a myriad of synthetic industrial goods,
40 refractory organic micropollutants, some of which act as endocrine disrupting chemicals
41 (EDCs), are frequently present in water bodies and eventually jeopardize living beings
42 health and ecosystems [1-4]. In the last decade, the electro-Fenton (EF) process has been
43 demonstrated to be highly effective and eco-friendly alike for the treatment of such
44 pollutants in wastewater [5,6]. The EF setups rely on the electrogeneration of H₂O₂ at
45 carbonaceous cathodes, which occurs with great faradaic efficiency from O₂ reduction
46 reaction. This in-situ reaction allows minimizing the dangers, hazards and costs
47 associated to industrial H₂O₂ synthesis [7-9]. The accumulated H₂O₂ is immediately
48 decomposed in the presence of Fe(II) catalyst, yielding abundant active hydroxyl radicals
49 (\bullet OH) in the bulk solution via Fenton's reaction [6]. Nonetheless, the large-scale
50 application of homogeneous EF (i.e., process in which free iron ions are used as catalyst)
51 is limited by the requirement of strict acidic pH and the gradual conversion of dissolved
52 iron into precipitate (mud) [10,11]. Lately, a strategy based in the use of solid iron-rich
53 materials as heterogeneous EF catalysts has gained momentum to minimize these
54 disadvantages, although new concerns have emerged in parallel [12]. The polyatomic
55 nature of the catalysts limits the exposure of iron active sites to H₂O₂, which must be
56 adsorbed prior to activation, and the relatively poor electron transfer between the reactants
57 (especially the restrained Fe(III)/Fe(II) redox cycling) is detrimental to the overall
58 catalytic performance [6,13]. Furthermore, the progressive deactivation and/or loss of
59 active iron sites affects the catalyst stability and durability, ending in nonviable materials
60 in practice [14,15]. It is thus evident that progress in design of catalysts with well-
61 balanced performance and stability is of major importance.

62 At present, the development of strong Fe-N ensembles embedded in carbon matrices
63 (denoted as Fe-N-C) is considered to be a promising strategy for the improvement of
64 activity, stability and reusability of the iron-based catalysts [16,17]. N-doping contributes
65 to the modulation of charge distribution of sp^2 -hybridized carbon framework and creates
66 new defects [18,19]. The electron-rich N sites coordinate with Fe atoms to form the so-
67 called FeN_x moieties [20], which exhibit fast electron transfer ability and are considered
68 as the actual active centers in many catalytic processes [21,22]. Moreover, the strong
69 binding between Fe and N atoms confers a greater stability to the metal active sites and
70 hence, to the whole catalyst during the given process [23]. As an example, Hu et al.
71 fabricated an iron-based catalyst with core-shell structure and abundant Fe_3C and FeN_x
72 sites; in an HEF system, the Fe_3C sites played a key role for H_2O_2 generation and FeN_x
73 promoted the H_2O_2 activation [13]. Other studies have revealed the role of various N-
74 functionalities present in the catalysts during the treatment of organic pollutants by
75 Fenton-based processes; pyrrolic N facilitates the adsorption of pollutants through π - π
76 and/or cation- π interactions, whereas N-doping eases the electron transfer through both
77 the external circuit and the carbon framework to enhance the Fe(III) reduction [8,9,24,25].
78 As a result, the electronic configuration of the π -conjugated ligands linked to FeN_4 sites
79 is relocated, which alters the rate-determining steps of the given reaction. In this regard,
80 FeN_4 sites have been proven superior as compared to other coordination geometries
81 (FeN_1 , FeN_2 and FeN_3) [26]. Unfortunately, for most Fe-N-C catalysts synthesized via
82 conventional pyrolysis routes, a large proportion of FeN_x moieties are hidden and
83 inaccessible to the reactants during the EF process, and the lack of strategies to precisely
84 modulate the coordination number in FeN_x moieties limits the overall activity.

85 Single-atom catalysts (SACs), with individual metal sites atomically dispersed on the
86 substrate, constitute a new frontier in catalysis. They have shown superior catalytic

87 performance as well as higher selectivity and stability in many research fields due to their
88 outstanding characteristics: unsaturated coordination configurations, fully exposed active
89 sites, strong metal-substrate interactions and quantum size effects [17,27-29]. The
90 application of Fe-SACs in advanced oxidation processes has become a very relevant
91 topic, as can be deduced from recent works: Chen and co-workers prepared Fe-SAC
92 anchored nitrogen-rich g-C₃N₄ nanotubes for peracetic acid activation by Fenton-like
93 reaction [30]; Xiong and co-workers fabricated an Fe-SAC using Fe(phen)₃ and SBA-15
94 as the precursors for peroxymonosulfate activation [31]; several authors reported the
95 application of Fe-SACs in HEF, trying to tune the multi-electron oxygen reduction
96 process to enable the O₂-to-•OH conversion [32-34]. Unfortunately, few studies address
97 the rational design of dense single-atom FeN₄ sites for water treatment by HEF process,
98 and the synthesis of SACs still remains challenging due to the easy aggregation of metal
99 atoms [35,36].

100 Metal-organic frameworks (MOFs), as ultraporous materials formed by the spatial
101 assembly of metal nodes and organic linkers, are common precursors to fabricate Fe-
102 SACs due to the large number of metal sites, ordered pores, large exposed surface and
103 diverse chemistry that is offered upon small structural changes [12,37,38]. Additionally,
104 nitrogen atoms from the organic linkers can promote the anchorage of the highly mobile
105 iron atoms, giving rise to strong FeN_x configurations [37,39-41]. Despite this, the
106 methodology still suffers from considerable aggregation of iron atoms because of the
107 carbon loss at high temperature [42]. This article addresses, for the first time, the rational
108 design of an Fe-SAC with robust FeN₄ moieties (Fe-SAC/NC) by the pyrolysis of a
109 surfactant-coordinated MOF, followed by the application to boost HEF treatment of
110 organic micropollutants in both model solution and urban wastewater. The involved
111 surfactant, cetyltrimethylammonium bromide, was able to regulate the crystallization of

112 the MOF precursor, coordinating with the surface metal sites to form a surfactant shell.
113 During the pyrolysis, the CTAB layers were decomposed into an N-doped carbon shell,
114 which acted as additional carbon and nitrogen source to stabilize the iron single-atom
115 sites and mitigate their agglomeration. Some density functional theory (DFT) calculations
116 are also included in this study, trying to elucidate the role of the single-atom FeN₄ sites.

117 **2. Materials and methods**

118 **2.1 Catalysts synthesis**

119 The synthesis route of Fe-SAC/NC is schematized in Fig. 1a. In brief, 1.00 g of
120 CTAB, 2.38 g of Zn(NO₃)₂•6H₂O and 1.10 g of FeSO₄•7H₂O were dissolved in 50 mL
121 methanol to form a clear solution. Then, 50 mL of methanol containing 3.63 g of 2-
122 methylimidazole were injected into the above mixture. After stirring for 30 min at 60 °C,
123 the resulting precipitate was centrifuged, sequentially cleaned with ethanol for several
124 times, and finally dried at 60 °C for 12 h. The resulting MOF was transferred into a tube
125 furnace to be heated at 900 °C for 3 h under nitrogen atmosphere. The carbonization
126 product was treated with 0.2 M HCl solution for 2 h at 50 °C, then cleaned with ethanol
127 and dried overnight. The final catalyst is denoted as Fe-SAC/NC or Fe₁/2Zn-1.0CTAB.
128 The preparation of catalysts with different CTAB dosage (0, 0.1, 0.5 and 1.5 g) followed
129 a similar procedure, and the obtained catalysts are denoted as Fe₁/2Zn-0CTAB (the
130 absence of surfactant gives rise to nanoparticle catalyst, Fe-NP/NC), Fe₁/2Zn-0.1CTAB,
131 Fe₁/2Zn-0.5CTAB and Fe₁/2Zn-1.5CTAB, respectively.

132 **2.2 Evaluation of catalytic performance**

133 The electrolytic assays were carried out in a single chamber glass cell that contained
134 160 mL of solution to be treated at room temperature. The cell was equipped with a gas-
135 diffusion electrode (GDE, 3 cm²) as cathode, with air supplied at 1 L min⁻¹ for constant

136 H₂O₂ production on site, and a Ti|IrO₂-based dimensionally stable plate (DSA, 3 cm²) or
137 a boron-doped diamond thin film (Si|BDD, 3 cm²) as the anode. The gap between the
138 anode and cathode was 1.0 cm. Constant current was applied using a DC power supply
139 (IT6302 from ITECH, China). The EF treatments were performed after catalyst addition.
140 Samples were obtained at selected times and immediately filtered with PTFE syringe
141 filters (0.22 μm) to remove particles. The degradation performance was evaluated by
142 measuring the concentration of pollutants using reversed-phase high performance liquid
143 chromatography (HPLC, SCION6000, China), as described in [Supplementary Material](#)
144 [\(SM\)](#).

145 **2.3 Characterization and Analytical Procedures**

146 Several techniques, including X-ray absorption near edge structure (XANES) and
147 extended X-ray absorption fine structure (EXAFS), high-resolution transmission electron
148 microscopy (HRTEM), X-ray photoelectron spectroscopy (XPS), X-ray diffraction
149 (XRD), thermogravimetric analysis (TGA), Raman analysis and inductively coupled
150 plasma (ICP) were employed to analyze the morphology, chemical and electronic
151 structures, and other properties of the synthesized materials. The details are given in [SM](#).
152 The analytical methods for determination of pH, H₂O₂ and dissolved iron concentrations,
153 and total organic carbon (TOC) are also explained in [SM](#).

154 **2.4 Computational Details**

155 Structural modelling and DFT calculations were carried out employing the Materials
156 Studio software package. The exchange-correlation interaction was described by
157 generalized gradient approximation (GGA) with the Perdew-Burke-Ernzerhof (PBE)
158 functional. The Brillouin zone was sampled by a Monkhorst-Pack 2 × 2 × 1 K-point grid.
159 The lattice constants were calculated using lattice parameters of 14.726 Å × 12.7825 Å ×
160 15.000 Å. The vacuum slab was set up to 15 Å. The geometric optimization was

161 terminated when the energy and force on each ion dropped below 10^{-5} Ha (3×10^{-4} eV)
162 and 0.002 Ha \AA^{-1} ($0.05\text{eV } \text{\AA}^{-1}$).

163 **3. Results and discussion**

164 **3.1 Characterization of the MOF-derived catalyst**

165 Fe-SAC/NC was prepared by carbonization of surfactant-coordinated Fe/ZIF-8
166 precursor at 900 °C under N_2 atmosphere (Fig. 1a). The surface Fe/Zn metal nodes in
167 ZIF-8 crystals can coordinate with the hydrophilic groups of CTAB to form surfactant
168 shells. The coordination-driven self-assembly slows down the crystal growth rate and
169 controls the shape and size of ZIF-8 crystals. During the pyrolysis, the surfactant layers
170 were the first ones to decompose at temperature from around 330 °C (Fig. S1), forming
171 ultrathin carbon layers at the surface. Finally, the zinc metal nodes were volatilized at
172 high temperature (boiling point at 907 °C), leaving atomically-anchored Fe on the N-
173 doped porous carbon matrices. Worth remarking, the cohesive interaction between CTAB
174 and MOF crystals allowed a confinement effect that suppressed the agglomeration of Fe
175 atoms, eventually yielding a large amount of atomically dispersed FeN_4 active sites.
176 Moreover, the N groups in CTAB provide additional N source to enhance the
177 coordination between Fe and N [43]. The TEM images depicted in Fig. 1b-d also confirm
178 the distinct carbon layer coating on the surface, and the catalyst partially inherited the
179 morphology of the MOF precursor, which may enhance the stability and the mass
180 transport during the reaction. The XRD patterns of Fe-SAC/NC and ZIF-8-derived N-
181 doped carbon matrices, as shown in Fig. 2a, exhibited only two peaks centered at 24.3°
182 and 44.5° , which were assigned to (002) and (004) crystal planes of carbon, respectively
183 [44,45]. No diffraction peak related to Fe-based species (iron oxides, iron nitrides or iron
184 carbides) appeared, evidencing that Fe sites were atomically dispersed in Fe-SAC/NC. In

185 contrast, a high amount of Fe atoms in the Fe-NP/NC, prepared in the absence of CTAB,
186 existed in the diffractogram of Fe₃N (Fig. 2b) [46].

187 Further evaluation of the coordination state and electronic features of Fe-SAC/NC is
188 crucial for in-depth understanding of the catalytic mechanisms underlying in the HEF
189 system. First, the XPS analysis was performed to reveal the chemical compositions and
190 the corresponding electronic states of the catalyst. The high resolution Fe 2*p* spectra of
191 Fe-NP/NC and Fe-SAC/NC (Fig. 2c) illustrate two splitting peaks at binding energies of
192 710.80 and 713.41 eV for the former material, which could be attributed to Fe(II) and
193 Fe(III) species, respectively [47,48]. However, both peaks in Fe-SAC/NC slightly shifted
194 to lower binding positions (710.16 and 712.77 eV), whereas the peak area of Fe(II)
195 increased to 63.3% compared to the 58.1% in Fe-NP/NC. These results are ascribed to
196 the introduction of CTAB, which enhances the dispersion of Fe atoms and the formation
197 of FeN_x moieties during the pyrolysis. Nitrogen from CTAB can bond with iron atoms
198 and decrease their electron density, thus enhancing the Fe(III) to Fe(II) conversion by
199 accelerating the electron transfer from carbon to iron sites [49,50]. Meanwhile, the
200 increase in the amount of carbon in Fe-SAC/NC (Fig. S2) further facilitated the
201 stabilization and reduction of Fe(III) atoms. Additionally, the Fe loading in Fe-SAC/NC
202 was measured by ICP as 8.5 wt%. In N 1*s* spectra (Fig. 2d), graphitic N (401.3 eV),
203 pyrrolic N (400.3 eV), Fe-N (399.7 eV), and pyridinic N (398.9 eV) were observed in
204 both samples [21,51-54]. Worth noting, the proportion of pyrrolic N was higher and Fe-
205 N was lower in Fe-SAC/NC as compared to Fe-NP/NC. As reported, Fe-N sites usually
206 act as the catalytic centers for the activation of H₂O₂ to form •OH, and pyrrolic N can
207 serve as adsorption sites for target pollutants during the wastewater treatment [13,55,56].
208 Therefore, higher amount of pyrrolic N and Fe-N may give rise to better catalytic
209 performance of the catalysts. In addition, the proportion of pyrrolic N and Fe-N was

210 greater with the increase of CTAB dosage during the synthesis, but excessive CTAB (i.e.,
211 1.5 g) led to the decrease in the proportion of pyrrolic N (Fig. 2e).

212 Further analysis of the surface defect states of Fe_{1/2}Zn-1.0CTAB and Fe_{1/2}Zn-
213 1.5CTAB was conducted by Raman spectroscopy. In Fig. 2f, two distinct peaks are
214 observed at 1350 cm⁻¹ and 1600 cm⁻¹, which are assigned to defective D and graphitic G
215 bands, respectively. These two peaks can be further deconvoluted into four peaks through
216 Gaussian numerical simulation, namely the sp²-type (at ~1350 cm⁻¹ and ~1600 cm⁻¹) and
217 the sp³-type carbon (at ~1200 cm⁻¹ and ~1500 cm⁻¹). And the integrated area ratio of sp³-
218 type/sp²-type carbon (A_{sp3}/A_{sp2}) enables the evaluation of the relative contents of
219 defective and graphitic carbon [57]. The I_D/I_G value, referring to the intensity ratio of the
220 D-band to G-band, was approximately 1.30 and 1.08 for Fe_{1/2}Zn-1.0CTAB and Fe_{1/2}Zn-
221 1.5CTAB, respectively, suggesting the formation of more lattice defects in the N-doped
222 porous carbon matrices of Fe_{1/2}Zn-1.0CTAB. In addition, the A_{sp3}/A_{sp2} value for
223 Fe_{1/2}Zn-1.0CTAB was as low as 0.38, which further demonstrates the high defective
224 degree and outstanding electronic conductivity [58,59]. As reported, the catalysts with
225 abundant defects are endowed with localized electrons, and the accelerated electron
226 transfer facilitates the dissociation of H₂O₂ to •OH and Fe(III)/Fe(II) redox cycling [60-
227 62].

228 The chemical states and local coordination environment of Fe atoms in Fe-SAC/NC
229 were investigated by XANES and EXAFS. Fig. 3a displays the normalized Fe K-edge
230 XANES spectra of the as-synthesized Fe-SAC/NC and the corresponding Fe foil, FeO
231 and Fe₂O₃ references. The increase in the valence of Fe would lead to the migration of the
232 rising edge to higher energy region [23]. As can be seen, the near-edge absorption energy
233 of the Fe K-edge for Fe-SAC/NC located between those of FeO and Fe₂O₃, indicating
234 that the Fe atoms in the sample carried a positive charge with the oxidation value between

235 +2 and +3. The Fourier transform extended X-ray absorption fine structure (FT-EXAFS)
236 spectrum of Fe-SAC/NC in Fig. 3b exhibits a prominent peak at ~ 1.6 Å, which can be
237 assigned to Fe-N bonds [63]. The typical peak for Fe-Fe scattering path, located at ~ 2.4
238 Å in the Fe foil, is absent in the spectrum of Fe-SAC/NC, providing solid evidence for
239 the absence of metallic iron clusters or nanoparticles in the sample. The EXAFS fitting
240 analysis further revealed the coordination environment of Fe in Fe-SAC/NC. The fitting
241 results in Fig. 3c and Table S2 verified that each Fe atom was coordinated by 4 N atoms
242 with the mean bond length of ~ 2.07 Å. Moreover, the EXAFS wavelet transform (WT)
243 plot of Fe-SAC/NC (Fig. 3d) only displayed an intensity maximum at 5.0 Å that is
244 associated with the Fe-N coordination, being clearly distinguished from the Fe-Fe
245 connection at 8.3 Å depicted in the plot of Fe foil. According to these results, it can be
246 concluded that the Fe-SAC/NC with robust single-atom FeN₄ sites was successfully
247 fabricated.

248 3.2 Evaluation of the catalytic activity of Fe-SAC/NC

249 To estimate the catalytic activity of the Fe-SAC/NC as a potential HEF catalyst, 2,4-
250 dichlorophenol (2,4-DCP) was selected as the target contaminant to be treated by different
251 processes (Fig. 4a). In electrochemical oxidation with in-situ generation of H₂O₂ at the
252 cathode (so-called EO-H₂O₂) [64], only a small 2,4-DCP removal of 17.3% in 90 min
253 was achieved. The adsorption efficiency of 2,4-DCP by Fe-SAC/NC was also as low as
254 15.6%. These results suggest the negligible contribution of anodic oxidation and
255 adsorption to 2,4-DCP removal. In contrast, complete abatement of 2,4-DCP was reached
256 by Fe-SAC/NC-catalyzed HEF process in 90 min, with extremely low iron leaching (1.23
257 mg L⁻¹), behaving much better than HEF with Fe-NP/NC catalyst that only allowed
258 attaining a 40.9% removal. The remarkable catalytic activity and stability of the Fe-
259 SAC/NC can be ascribed to the abundant accessible single-atom FeN₄ sites.

260 Since the chemical states and electronic features of the catalysts may vary under
261 different synthesis conditions, the catalysts prepared with different amount of CTAB
262 source were tested in the HEF treatment of 2,4-DCP. As depicted in Fig. 4b, Fe₁/2Zn-
263 1.0CTAB exhibited the best activity in terms of 2,4-DCP degradation, attaining a 99.3%
264 removal at 60 min, being superior to Fe₁/2Zn-1.5CTAB (95.3%), Fe₁/2Zn-0.5CTAB
265 (60.9%) and Fe₁/2Zn-0.1CTAB (47.1%). As described in Fig. S3, the proportion of
266 different N species in the catalyst highly depended on the dosage of CTAB and, among
267 them, Fe-N and pyrrolic N may play significant roles in the removal of 2,4-DCP.
268 Therefore, the relationship between the kinetic constants for the degradation of 2,4-DCP
269 and the relative contents of Fe-N and pyrrolic N in the catalysts can be inferred from data
270 shown in Fig. 4c and Fig. 2e, respectively. The increase in the CTAB dose from 0.1 to 1.0
271 g led to growing percentages of Fe-N and pyrrolic N, which also yielded quicker 2,4-DCP
272 disappearance. The results verify again the positive effect of Fe-N and pyrrolic N on the
273 catalytic performance. However, further increase of the CTAB dosage to 1.5 g was
274 detrimental, evidenced from the less effective 2,4-DCP abatement. This was due to the
275 fact that excessive CTAB hinders the nucleation and growth of ZIF-8 precursor, then
276 hampering the formation of single-atom FeN₄ sites despite the increase in the Fe-N
277 content.

278 The effect of various operation parameters, including pH, catalyst dosage and applied
279 current, on the 2,4-DCP concentration decay upon the application of Fe-SAC/NC-
280 catalyzed HEF treatment was explored. As expected, increasing the catalyst dosage from
281 0.05 to 0.20 g L⁻¹ allowed the substantial enhancement of 2,4-DCP concentration decay
282 (Fig. 4d). Notably, a dramatic increase in the 2,4-DCP removal was achieved when the
283 catalyst dosage was increased from 0.05 to 0.10 g L⁻¹, with only a small rise in iron
284 leaching (i.e., 0.26 mg L⁻¹, see inset), indicating that the greater catalytic performance

285 was due to the increased amount of single-atom FeN₄ active sites rather than the
286 homogeneous Fenton's reaction by the dissolved iron ions. As shown in Fig. 4e, the
287 quickest decay of 2,4-DCP was observed at initial pH 3.0, and the degradation efficiency
288 was gradually decreased with the increase in pH value. The enhanced performance at
289 more acidic pH is logically attributed to the higher oxidation potential of •OH at low pH,
290 as well as the contribution of homogeneous Fenton's reaction occurring from dissolved
291 iron ions (Fig. 4f). In other words, the loss of atomically dispersed iron sites at strong
292 acidic pH would reduce the recyclability of Fe-SAC/NC. Fortunately, 100% and 96.8 %
293 2,4-DCP removal could be still obtained at initial pH 4.0 and 5.0 with low iron leaching
294 of 1.23 and 0.96 mg L⁻¹, respectively, corroborating both the high activity and stability of
295 the catalyst at near-neutral pH. Fig. S4 illustrates the positive effect of applied current
296 increase on pollutant removal. The higher current gave rise to greater H₂O₂ accumulation
297 in the bulk and, consequently, to a higher amount of •OH. The catalytic performance of
298 Fe-SAC/NC-based HEF system was further investigated by treating several organic
299 pollutants separately. As illustrated in Fig. 5a, the complete degradation of Rhodamine B,
300 trimethylolpropane and ciprofloxacin and more than 90% removal of Methyl Orange can
301 be observed in 30 min, whereas other pollutants were also completely removed in 60 min.
302 Such results can be explained by the unique feature of •OH, being nonselective in the
303 degradation of most organics. Besides, the physicochemical properties of the organics,
304 such as molecular structure and electron affinity, can affect their adsorption and
305 decomposition, leading to different kinetic constants (Fig. 5a).

306 **3.3 Recyclability and applicability of Fe-SAC/NC**

307 Apart from the catalytic activity, the recyclability of the Fe-SAC/NC was also
308 assessed from cycling tests. As depicted in Fig. 5b, the complete removal profiles of 2,4-
309 DCP remained unaltered after five successive runs, demonstrating the remarkable

310 recyclability of Fe-SAC/NC. The leached iron concentration was 1.23 mg L^{-1} at the first
311 cycle, then being undetectable after the second run. The slight decrease in the degradation
312 kinetic constant, especially in the fourth and fifth runs, informs about certain deactivation
313 of catalyst due to the loss of FeN_4 active sites and the adsorption of some organic
314 intermediates on the surface during the long-term operation. The optimization of the
315 cleaning procedure based on organic solvent and weak acid solution may increase its
316 regeneration.

317 The applicability of Fe-SAC/NC in real cases was further evaluated by treating 2,4-
318 DCP in urban wastewater at initial pH 4.0 (Fig. 5c). The almost total disappearance of
319 2,4-DCP at 90 min is evidenced, being the removal slower than that in simulated aqueous
320 matrix due to the competition of other organics in wastewater for the $\bullet\text{OH}$ [56]. Moreover,
321 the mineralization ability of Fe-SAC/NC-catalyzed HEF process was assessed from TOC
322 analysis. In Fig. 5d, it can be seen that the BDD/air-diffusion cell achieved a substantial
323 mineralization of 67.6% at 300 min, outperforming that with a RuO_2 -based DSA anode
324 thanks to the production of physisorbed BDD($\bullet\text{OH}$) [65]. Consequently, the Fe-SAC/NC-
325 catalyzed HEF system owns an interesting recyclability and applicability.

326 **3.4 Mechanistic Insights**

327 The electrochemical impedance spectroscopy (EIS) Nyquist plots were obtained to
328 evaluate the ability of the Fe-SAC/NC to shuttle and conduct the surface charge (Fig. S5).
329 The R_{ct} value (inset), which is related to the charge-transfer resistance of the catalyst, was
330 acquired from the fitting of the corresponding equivalent circuit [66,67]. The results in
331 Fig. S5 revealed that the R_{ct} values for Fe-SAC/CN and Fe-NP/CN were 3.44 and 7.10
332 $\text{k}\Omega$, respectively, demonstrating the enhanced charge transfer efficiency of Fe-SAC/NC
333 due to the addition of CTAB during the synthesis.

334 DFT calculations on the Gibbs free energy during H₂O₂ adsorption and activation by
335 the FeN₄ or Fe₃N sites were carried out comparatively to provide insights into the catalytic
336 mechanisms. The details are shown in Fig. 6a. The H₂O₂ molecule is first adsorbed on the
337 top of the iron site (FeN₄ or Fe₃N) with one of the O atoms bound to the iron atom
338 (H₂O₂*). The HOO-FeN₄ or HOO-Fe₃N bond (HOO*) is then achieved by releasing one
339 proton. Finally, the O-O bond of the intermediate HOO* is broken to yield the HO*
340 species, which can be desorbed from the catalyst quickly to degrade the organic molecules
341 [59,68,69]. The superior catalytic activity of Fe-SA/NC over Fe-NP/NC for HEF can be
342 ascribed to two facts: (i) the desorption step to yield •OH species in Fe-SAC/NC is an
343 exothermal reaction and a feasible process, whereas the formation of the same oxidant
344 from HO-FeN₄ bond is an endothermal reaction (Fig. 6, right plot); (ii) the Gibbs free
345 energy difference value of Fe-SAC/NC ($\Delta G = -3.110$ eV) is greater than that of Fe-NP/NC
346 ($\Delta G = -2.758$ eV) during the breakage of HOO* to HO*, indicating the easier cleavage
347 of H₂O₂ to form •OH. Such differences confirm the excellent activity of single-atom FeN₄
348 sites towards H₂O₂ activation, in full agreement with the previous experimental results.

349 Based on the above findings, a detailed mechanism explaining the superior
350 performance of Fe-SAC/NC-catalyzed HEF treatment of 2,4-DCP (also valid for other
351 organic pollutants) is proposed (Fig. 7). First, the in-situ generated H₂O₂ at the cathode
352 can be efficiently adsorbed at the FeN₄ sites; then, it is rapidly decomposed to form a
353 large number of •OH via the interaction between H₂O₂ and FeN₄ sites. Meanwhile, the
354 pyrrolic N in the catalyst favors the adsorption of the pollutant through the π - π and/or
355 cation- π interactions. The enhanced mass transport decreases the migration distance
356 between •OH and target 2,4-DCP molecules, resulting in the efficient degradation of the
357 pollutant. As the reactions proceed, the single-atom FeN₄ sites undergo repetitive
358 interconversion of the states during H₂O₂ adsorption and activation, leading to excellent

359 catalytic performance. On the other hand, the ultrathin carbon layer derived from CTAB
360 not only suppresses the agglomeration of iron atoms, but also facilitates the formation of
361 robust FeN₄ moieties during the synthesis. The coordination between Fe and N actually
362 decreases the electron density of iron sites due to the high electronegativity of N element,
363 which accelerates the Fe(III)/Fe(II) redox cycling during the treatment.

364 **4. Conclusions**

365 Robust single-atom FeN₄ sites anchored on an N-doped carbon matrix were
366 successfully prepared for the efficient HEF treatment of 2,4-DCP and other organic
367 pollutants. Complete abatement of 2,4-DCP was attained by Fe-SAC/NC-catalyzed HEF
368 process at 90 min, with very low iron leaching (1.23 mg L⁻¹), which was superior to HEF
369 with Fe-NP/NC catalyst that only allowed 41% 2,4-DCP removal. The Fe-SAC/NC
370 exhibited reasonable stability and recyclability in HEF system. The dominant role of FeN₄
371 sites was verified from the thorough catalyst characterization and the experimental assays
372 and DFT calculations. The modulation of the electronic structure of the catalyst by
373 constructing dense FeN₄ moieties facilitated the electron transfer to yield a larger amount
374 of •OH during the HEF, whereas the adjacent pyrrolic N enhanced the adsorption of target
375 organic pollutants. These findings provide new insights into the rational design of highly
376 active, stable, and multi-functional HEF catalysts, and inspire the exploration and
377 application of electrochemical advanced oxidation technologies for real wastewater
378 treatment.

379 **Acknowledgment**

380 The authors gratefully acknowledge financial support from the National Natural
381 Science Foundation of China (No. 52100073), the Fundamental Research Funds for the
382 Central Universities (2021CDJQY-054, China), Venture and Innovation Support
383 Program for Chongqing Over-seas Returnees (cx2022048, China) and project PID2019-

384 109291RB-I00 (MCIN/AEI/10.13039/501100011033, Spain). The PhD scholarship
385 awarded to L.Z. (State Scholarship Fund, CSC, China) is also acknowledged.

386 **References**

- 387 [1] E. Mousset, Y. Pechaud, N. Oturan, M.A. Oturan, Charge transfer/mass transport
388 competition in advanced hybrid electrocatalytic wastewater treatment: Development
389 of a new current efficiency relation, *Appl. Catal. B: Environ.* 240 (2019) 102-111.
390 <https://doi.org/10.1016/j.apcatb.2018.08.055>
- 391 [2] V.H. Nguyen, S.M. Smith, K. Wantala, P. Kajitvichyanukul, Photocatalytic
392 remediation of persistent organic pollutants (POPs): a review, *Arab. J. Chem.* 13
393 (2020) 8309-8337. <https://doi.org/10.1016/j.arabjc.2020.04.028>
- 394 [3] S.O. Ganiyu, C.A. Martínez-Huitle, M.A. Oturan, Electrochemical advanced
395 oxidation processes for wastewater treatment: Advances in formation and detection
396 of reactive species and mechanisms, *Curr. Opin. Electrochem.* 27 (2021) 100678.
397 <https://doi.org/10.1016/j.coelec.2020.100678>
- 398 [4] E. Brillas, Progress of homogeneous and heterogeneous electro-Fenton treatments of
399 antibiotics in synthetic and real wastewaters: A critical review on the period 2017-
400 2021, *Sci. Total Environ.* 819 (2022) 153102.
401 <https://doi.org/10.1002/celc.202100588>
- 402 [5] N. Oturan, J. Bo, C. Trelu, M.A. Oturan, Comparative performance of ten electrodes
403 in electro-Fenton process for removal of organic pollutants in water,
404 *ChemElectroChem* 8 (2021) 3294-3303. <https://doi.org/10.1002/celc.202100588>
- 405 [6] I. Sirés, E. Brillas, Upgrading and expanding the electro-Fenton and related processes,
406 *Curr. Opin. Electrochem.* 227 (2021) 100686.
407 <https://doi.org/10.1016/j.coelec.2020.100686>

- 408 [7] H. Roth, Y. Gendel, P. Buzatu, O. David, M. Wessling, Tubular carbon nanotube-
409 based gas diffusion electrode removes persistent organic pollutants by a cyclic
410 adsorption-electro-Fenton process, *J. Hazard. Mater.* 307 (2016) 1-6.
411 <https://doi.org/10.1016/j.jhazmat.2015.12.066>
- 412 [8] G. Daniel, Y. Zhang, S. Lanzalaco, F. Brombin, T. Kosmala, G. Granozzi, A. Wang,
413 E. Brillas, I. Sirés, C. Durante, Chitosan-derived nitrogen-doped carbon
414 electrocatalyst for a sustainable upgrade of oxygen reduction to hydrogen peroxide
415 in UV-assisted electro-Fenton water treatment, *ACS Sustain. Chem. Eng.* 8 (2020)
416 14425-14440. <https://doi.org/10.1021/acssuschemeng.0c04294>
- 417 [9] Y. Zhang, G. Daniel, S. Lanzalaco, A.A. Issec, A. Facchini, A. Wang, E. Brillas, C.
418 Durante, I. Sirés, H₂O₂ production at gas-diffusion cathodes made from agarose-
419 derived carbons with different textural properties for acetaminophen degradation in
420 chloride media, *J. Hazard. Mater.* 423 (2022) 127005.
421 <https://doi.org/10.1016/j.jhazmat.2021.127005>
- 422 [10] F.C. Moreira, R.A.R. Boaventura, E. Brillas, V.J.P. Vilar, Electrochemical advanced
423 oxidation processes: A review on their application to synthetic and real wastewaters,
424 *Appl. Catal. B: Environ.* 202 (2017) 217-261.
425 <https://doi.org/10.1016/j.apcatb.2016.08.037>
- 426 [11] M. Pacheco-Álvarez, R.P. Benítez, O.M. Rodríguez-Narváez, E. Brillas, J.M.
427 Peralta-Hernández, A critical review on paracetamol removal from different aqueous
428 matrices by Fenton and Fenton-based processes, and their combined methods,
429 *Chemosphere* 303 (2022) 134883.
430 <https://doi.org/10.1016/j.chemosphere.2022.134883>
- 431 [12] S.O. Ganiyu, M. Zhou, C.A. Martínez-Huitle, Heterogeneous electro-Fenton and
432 photoelectro-Fenton processes: A critical review of fundamental principles and

- 433 application for water/wastewater treatment, *Appl. Catal. B: Environ.* 235 (2018)
434 103-129. <https://doi.org/10.1016/j.apcatb.2018.04.044>
- 435 [13] J. Hu, S. Wang, J. Yu, W. Nie, J. Sun, S. Wang, Duet Fe₃C and FeN_x sites for H₂O₂
436 generation and activation toward enhanced electro-Fenton performance in
437 wastewater treatment, *Environ. Sci. Technol.* 55 (2021) 1260-1269.
438 <https://doi.org/10.1021/acs.est.0c06825>
- 439 [14] V. Poza-Nogueiras, E. Rosales, M. Pazos, M.A. Sanroman, Current advances and
440 trends in electro-Fenton process using heterogeneous catalysts-A review,
441 *Chemosphere* 201 (2018) 399-416.
442 <https://doi.org/10.1016/j.chemosphere.2018.03.002>
- 443 [15] Z. Ye, G.E.M. Schukraft, A. L'Hermitte, Y. Xiong, E. Brillas, C. Petit, I. Sirés,
444 Mechanism and stability of an Fe-based 2D MOF during the photoelectro-Fenton
445 treatment of organic micropollutants under UVA and visible light irradiation, *Water*
446 *Res.* 184 (2020) 115986. <https://doi.org/10.1016/j.watres.2020.115986>
- 447 [16] B. Singh, M.B. Gawande, A.D. Kute, R.S. Varma, P. Fornasiero, P. McNeice, R.V.
448 Jagadeesh, R. Beller, R. Zbořil, Single-atom (iron-based) catalysts: Synthesis and
449 applications, *Chem. Rev.* 121 (2021) 13620-13697.
450 <https://doi.org/10.1021/acs.chemrev.1c00158>
- 451 [17] Y. Shang, X. Duan, S. Wang, Q. Yue, B. Gao, X. Xu, Carbon-based single atom
452 catalyst: Synthesis, characterization, DFT calculations, *Chinese Chem. Lett.* 33
453 (2021) 663-673. <https://doi.org/10.1016/j.ccllet.2021.07.050>
- 454 [18] H. Yu, Y. Xue, Y. Li, Graphdiyne and its assembly architectures: synthesis,
455 functionalization, and applications, *Adv. Mater.* 31 (2019) 1803101.
456 <https://doi.org/10.1002/adma.201803101>

- 457 [19] K. Tian, J. Wang, L. Cao, W. Yang, W. Guo, S. Liu, W. Li, F. Wang, X. Li, Z. Xu,
458 Z. Wang, H. Wang, Y. Huo, Single-site pyrrolic-nitrogen-doped sp(2)-hybridized
459 carbon materials and their pseudocapacitance, *Nat. Commun.* 11 (2020) 3884.
460 <https://doi.org/10.1038/s41467-020-17727-y>
- 461 [20] W. Miao, Y. Liu, D. Wang, N. Du, Z. Ye, Y. Hou, S. Mao, K. Ostrikov, The role of
462 Fe-N_x single-atom catalytic sites in peroxymonosulfate activation: Formation of
463 surface-activated complex and non-radical pathways, *Chem. Eng. J.* 423 (2021)
464 130250. <https://doi.org/10.1016/j.cej.2021.130250>
- 465 [21] X. Xie, L. Peng, H. Yang, G.I.N. Waterhouse, L. Shang, T. Zhang, MIL-101-derived
466 mesoporous carbon supporting highly exposed Fe single-atom sites as efficient
467 oxygen reduction reaction catalysts, *Adv. Mater.* 33 (2021) 2101038.
468 <https://doi.org/10.1002/adma.202101038>
- 469 [22] L. Yu, Y. Li, Y. Ruan, Dynamic control of sacrificial bond transformation in the Fe-
470 N-C single-atom catalyst for molecular oxygen reduction, *Angew. Chem. Int. Ed.*
471 60 (2021) 25296-25301. <https://doi.org/10.1002/ange.202111761>
- 472 [23] X. Peng, J. Wu, Z. Zhao, X. Wang, H. Dai, L. Xu, G. Xu, Y. Jian, F. Hu, Activation
473 of peroxymonosulfate by single-atom Fe-g-C₃N₄ catalysts for high efficiency
474 degradation of tetracycline via nonradical pathways: Role of high-valent iron-oxo
475 species and Fe-N_x sites, *Chem. Eng. J.* 427 (2022) 130803.
476 <https://doi.org/10.1016/j.cej.2021.130803>
- 477 [24] X. Li, X. Huang, S. Xi, S. Miao, J. Ding, W. Cai, S. Liu, X. Yang, H. Yang, J. Gao,
478 J. Wang, Y. Huang, T. Zhang, B. Liu, Single cobalt atoms anchored on porous N-
479 doped graphene with dual reaction sites for efficient Fenton-like catalysis, *J. Am.*
480 *Chem. Soc.* 140 (2018) 12469-12475. <https://doi.org/10.1021/jacs.8b05992>

- 481 [25] J. Yu, Z. Zhu, H. Zhang, Y. Qiu, D. Yin, Fe-nitrogen-doped carbon with dual active
482 sites for efficient degradation of aromatic pollutants via peroxymonosulfate
483 activation, Chem. Eng. J. 427 (2022) 130898.
484 <https://doi.org/10.1016/j.cej.2021.130898>
- 485 [26] Y. Li, X. Liu, L. Zheng, J. Shang, X. Wan, R. Hu, X. Guo, S. Hong, J. Shui,
486 Preparation of Fe-N-C catalysts with FeN_x (x = 1, 3, 4) active sites and comparison
487 of their activities for the oxygen reduction reaction and performances in proton
488 exchange membrane fuel cells, J. Mater. Chem. A 7 (2019) 26147-26153.
489 <https://doi.org/10.1039/C9TA08532G>
- 490 [27] I.S. Pieta, R.G. Kadam, P. Pieta, D. Mrdenovic, R. Nowakowski, A. Bakandritsos,
491 M. Petr, M. Otyepka, R. Kostecki, M.A.M. Khan, R. Zboril, M.B. Gawande, The
492 hallmarks of copper single atom catalysts in direct alcohol fuel cells and
493 electrochemical CO₂ fixation, Adv. Mater. Interfaces 8 (2021) 2001822.
494 <https://doi.org/10.1002/admi.202001822>
- 495 [28] R.G. Kadam, T. Zhang, D. Zaoralová, M. Medved', A. Bakandritsos, O. Tomanec,
496 M. Petr, J.Z. Chen, J.T. Miller, M. Otyepka, R. Zbořil, T. Asefa, M.B. Gawande,
497 Single Co-atoms as electrocatalysts for efficient hydrazine oxidation reaction, Small
498 17 (2021) 2006477. <https://doi.org/10.1002/smll.202006477>
- 499 [29] P. Sharma, S. Kumar, O. Tomanec, M. Petr, J.Z. Chen, J.T. Miller, R.S. Varma, M.B.
500 Gawande, R. Zbořil, Carbon nitride-based ruthenium single atom photocatalyst for
501 CO₂ reduction to methanol, Small 17 (2021) 2006478.
502 <https://doi.org/10.1002/smll.202006478>
- 503 [30] F. Chen, L. Liu, J. Wu, X. Rui, J. Chen, Y. Yu, Single-atom iron anchored tubular
504 g-C₃N₄ catalysts for ultrafast Fenton-like reaction: Roles of high-valency iron-oxo

505 species and organic radicals, *Adv. Mater.* 34 (2022) 2202891.
506 <https://doi.org/10.1002/adma.202202891>

507 [31] Y. Xiong, H. Li, C. Liu, L. Zheng, C. Liu, J. Wang, S. Liu, Y. Han, L. Gu, J. Qian,
508 D. Wang, Single-atom Fe catalysts for Fenton-like reactions: Roles of different N
509 species, *Adv. Mater.* 34 (2022) 2110653. <https://doi.org/10.1002/adma.202110653>

510 [32] P. Cao, X. Quan, K. Zhao, S. Chen, H. Yu, Y. Su, High-efficiency electrocatalysis
511 of molecular oxygen toward hydroxyl radicals enabled by an atomically dispersed
512 iron catalyst, *Environ. Sci. Technol.* 54 (2020) 12662-12672.
513 <https://doi.org/10.1021/acs.est.0c03614>

514 [33] K. Zhao, X. Quan, Y. Su, X. Qin, S. Chen, H. Yu, Enhanced chlorinated pollutant
515 degradation by the synergistic effect between dechlorination and hydroxyl radical
516 oxidation on a bimetallic single-atom catalyst, *Environ. Sci. Technol.* 55 (2021)
517 14194-14203. <https://doi.org/10.1021/acs.est.1c04943>

518 [34] D. Zhang, K. Yin, Y. Tang, Y. Wei, H. Tang, H. Liu, Y. Chen, C. Liu, Hollow sea-
519 urchin-shaped carbon-anchored single-atom iron as dual-functional electro-Fenton
520 catalysts for degrading refractory thiamphenicol with fast reaction kinetics in a wide
521 pH range, *Chem. Eng. J.* 427 (2022) 130996.
522 <https://doi.org/10.1016/j.cej.2021.130996>

523 [35] M. Liu, J. Lee, T. Yang, F. Zheng, J. Zhao, C. Yang, L.Y.S. Lee, Synergies of Fe
524 single atoms and clusters on N-doped carbon electrocatalyst for pH-universal
525 oxygen reduction, *Small Methods* 5 (2021) 001165.
526 <https://doi.org/10.1002/smtd.202001165>

527 [36] L. Peng, X. Duan, Y. Shang, B. Gao, X. Xu, Engineered carbon supported single
528 iron atom sites and iron clusters from Fe-rich enteromorpha for Fenton-like reactions

529 via nonradical pathways, *Appl. Catal. B: Environ.* 287 (2021) 119963.
530 <https://doi.org/10.1016/j.apcatb.2021.119963>

531 [37] T.A. Goetjen, J. Liu, Y. Wu, J. Sui, X. Zhang, J.T. Hupp, O.K. Farha, Metal-organic
532 framework (MOF) materials as polymerization catalysts: a review and recent
533 advance, *Chem. Commun.* 56 (2020) 10409-10418.
534 <https://doi.org/10.1039/D0CC03790G>

535 [38] K. Dashtian, S. Shahbazi, M. Tayebi, Z. Masoumi, A review on metal-organic
536 frameworks photoelectrochemistry: A headlight for future applications, *Coord.*
537 *Chem. Rev.* 445 (2021) 214097. <https://doi.org/10.1016/j.ccr.2021.214097>

538 [39] A. Han, B. Wang, A. Kumar, Y. Qin, J. Jin, X. Wang, C. Yang, B. Dong, Y. Jia, J.
539 Liu, X. Sun, Recent advances for MOF-derived carbon-supported single-atom
540 catalysts, *Small Methods* 3 (2019) 1800471.
541 <https://doi.org/10.1002/smtd.201800471>

542 [40] Z. Song, L. Zhang, K. Doyle-Davis, X. Fu, J. Luo, X. Sun, Recent advances in MOF-
543 derived single atom catalysts for electro Recent advances for MOF-derived carbon-
544 supported single-atom catalysts chemical applications, *Adv. Energy Mater.* 10
545 (2020) 2001561. <https://doi.org/10.1002/aenm.202001561>

546 [41] Y. Wei, M. Zhang, R. Zou, Q. Xu, Metal-organic framework-based catalysts with
547 single metal sites, *Chem. Rev.* 120 (2020) 12089-12174.
548 <https://doi.org/10.1021/acs.chemrev.9b00757>

549 [42] X. Chen, N. Wang, K. Shen, Y. Xie, Y. Tan, Y. Li, MOF-derived isolated Fe atoms
550 implanted in N-doped 3D hierarchical carbon as an efficient ORR electrocatalyst in
551 both alkaline and acidic media, *ACS Appl. Mater. Inter.* 11 (2019) 25976-25985.
552 <https://doi.org/10.1021/acsami.9b07436>

- 553 [43] Y. He, S. Hwang, D.A. Cullen, M.A. Uddin, L. Langhorst, B. Li, S. Karakalos, A.J.
554 Kropf, E.C. Wegener, J. Sokolowski, Highly active atomically dispersed CoN₄ fuel
555 cell cathode catalysts derived from surfactant-assisted MOFs: carbon-shell
556 confinement strategy, *Energy Environ. Sci.* 12 (2019) 250-260.
557 <https://doi.org/10.1039/C8EE02694G>
- 558 [44] X. Wang, C. Yang, X. Wang, H. Zhu, L. Cao, A. Chen, L. Gu, Q. Zhang, L. Zheng,
559 H. Liang, Green synthesis of a highly efficient and stable single-atom iron catalyst
560 anchored on nitrogen-doped carbon nanorods for the oxygen reduction reaction,
561 *ACS Sustain. Chem. Eng.* 9 (2020) 137-146.
562 <https://doi.org/10.1021/acssuschemeng.0c05509>
- 563 [45] L. Zhou, P. Zhou, Y. Zhang, B. Liu, P. Gao, S. Guo, 3D star-like atypical hybrid
564 MOF derived single-atom catalyst boosts oxygen reduction catalysis, *J. Energy*
565 *Chem.* 55 (2021) 355-360. <https://doi.org/10.1016/j.jechem.2020.06.059>
- 566 [46] J. Xiao, J. Chen, Z. Ou, J. Lai, T. Yu, Y. Wang, N-doped carbon-coated Fe₃N
567 composite as heterogeneous electro-Fenton catalyst for efficient degradation of
568 organics, *Chinese J. Catal.* 42 (2021) 953-962. [https://doi.org/10.1016/S1872-](https://doi.org/10.1016/S1872-2067(20)63719-6)
569 [2067\(20\)63719-6](https://doi.org/10.1016/S1872-2067(20)63719-6)
- 570 [47] X. Du, W. Fu, P. Su, L. Su, Q. Zhang J. Cai, M. Zhou, Trace FeCu@ PC derived
571 from MOFs for ultraefficient heterogeneous electro-Fenton process: Enhanced
572 electron transfer and bimetallic synergy, *ACS ES&T Eng.* 1 (2021) 1311-1322.
573 <https://doi.org/10.1021/acsestengg.1c00131>
- 574 [48] Y. Gao, X. Duan, B. Li, Q. Jia, Y. Li, X. Fan, F. Zhang, G. Zhang, S. Wang, W.
575 Peng, Fe containing templates derived atomic Fe-NC to boost Fenton-like reaction
576 and the charge migration analysis on highly active Fe-N₄ sites, *J. Mater. Chem. A* 9
577 (2021) 14793-14805. <https://doi.org/10.1039/D1TA02446A>

- 578 [49] Y. Li, X. Wei, L. Chen, J. Shi, M. He, Nickel-molybdenum nitride nanoplate
579 electrocatalysts for concurrent electrolytic hydrogen and formate productions, Nat.
580 Commun. 10 (2019) 1-12. <https://doi.org/10.1038/s41467-019-13375-z>
- 581 [50] T. Yang, D. Yu, D. Wang, T. Yang, Z. Li, M. Wu, M. Petru, J. Crittenden,
582 Accelerating Fe(III)/Fe(II) cycle via Fe(II) substitution for enhancing Fenton-like
583 performance of Fe-MOFs, Appl. Catal. B: Environ. 286 (2021) 119859.
584 <https://doi.org/10.1016/j.apcatb.2020.119859>
- 585 [51] K. Yuan, S. Sfaelou, M. Qiu, D. Lützenkirchen-Hecht, X. Zhuang, Y. Chen, C. Yuan,
586 X. Feng, U. Scherf, Synergetic contribution of boron and Fe-N_x species in porous
587 carbons toward efficient electrocatalysts for oxygen reduction reaction, ACS Energy
588 Lett. 3 (2017) 252-260. <https://doi.org/10.1021/acsenergylett.7b01188>
- 589 [52] J. Han, X. Meng, L. Lu, J. Bian, Z. Li, C. Sun, Single-atom Fe-N_x-C as an efficient
590 electrocatalyst for zinc-air batteries, Adv. Funct. Mater. 29 (2019) 1808872.
591 <https://doi.org/10.1002/adfm.201808872>
- 592 [53] T. Yang, S. Fan, Y. Li, Q. Zhou, Fe-N/C single-atom catalysts with high density of
593 Fe-N_x sites toward peroxymonosulfate activation for high-efficient oxidation of
594 bisphenol A: Electron-transfer mechanism, Chem. Eng. J. 419 (2021) 129590.
595 <https://doi.org/10.1016/j.cej.2021.129590>
- 596 [54] S. Ren, X. Duan, M. Lei, S. Liang, M. Zhang, H. Zheng, Energetic MOF-derived
597 cobalt/iron nitrides embedded into N,S-codoped carbon nanotubes as superior
598 bifunctional oxygen catalysts for Zn-air batteries, Appl. Surf. Sci. 569 (2021)
599 151030. <https://doi.org/10.1016/j.apsusc.2021.151030>
- 600 [55] J. Yang, D. Zeng, Q. Zhang, R. Cui, M. Hassan, L. Dong, J. Li, Y. He, Single Mn
601 atom anchored on N-doped porous carbon as highly efficient Fenton-like catalyst for

602 the degradation of organic contaminants, *Appl. Catal. B: Environ.* 279 (2020)
603 119363. <https://doi.org/10.1016/j.apcatb.2020.119363>

604 [56] J. Yang, D. Zeng, J. Li, L. Dong, W. Ong, Y. He, A highly efficient Fenton-like
605 catalyst based on isolated diatomic Fe-Co anchored on N-doped porous carbon,
606 *Chem. Eng. J.* 404 (2021) 126376. <https://doi.org/10.1016/j.cej.2020.126376>

607 [57] Z. Zhu, F. Cheng, J. Chen, Investigation of effects of carbon coating on the
608 electrochemical performance of $\text{Li}_4\text{Ti}_5\text{O}_{12}/\text{C}$ nanocomposites, *J. Mater. Chem. A* 1
609 (2013) 9484-9490. <https://doi.org/10.1039/C3TA00114H>

610 [58] W. Duan, Z. Hu, K. Zhang, F. Cheng, Z. Tao, J. Chen, $\text{Li}_3\text{V}_2(\text{PO}_4)_3/\text{C}$ core-shell
611 nanocomposite as a superior cathode material for lithium-ion batteries, *Nanoscale* 5
612 (2013) 6485-6490. <https://doi.org/10.1039/C3NR01617J>

613 [59] F. Wang, N. Zhang, X. Zhao, L. Wang, J. Zhang, T. Wang, F. Liu, Y. Liu, L. Fan,
614 Realizing a high-performance Na-storage cathode by tailoring ultrasmall
615 $\text{Na}_2\text{FePO}_4\text{F}$ nanoparticles with facilitated reaction kinetics, *Adv Sci.* 6 (2019)
616 1900649. <https://doi.org/10.1002/advs.201900649>

617 [60] L. Zhou, Q. Chang, C. Xue, N. Li, C. Hao, J. Yang, S. Hu, Graphitic carbon nitride
618 modified with trace-level copper and carbon dots exhibits excellent photo-Fenton
619 catalytic activity with low consumption of H_2O_2 , *Ceram. Int.* 48 (2022) 17960-17968.
620 <https://doi.org/10.1016/j.ceramint.2022.04.126>

621 [61] H. Qi, X. Sun, Z. Sun, Porous graphite felt electrode with catalytic defects for
622 enhanced degradation of pollutants by electro-Fenton process, *Chem. Eng. J.* 403
623 (2021) 126270. <https://doi.org/10.1016/j.cej.2020.126270>

624 [62] Z. Wang, L. Pi, J. Cui, X. Zhang, Y. Liu, D. Tang, H. Zhu, X. Mao, Heterogeneous
625 electro-Fenton system for efficient degradation of 2,4-DCP: Dual activation of O_2

626 for H₂O₂ generation and oxygen-defect cobalt ferrite catalyst. *Sep. Purif. Technol.*
627 255 (2021) 117731. <https://doi.org/10.1016/j.seppur.2020.117731>

628 [63] K. Qian, H. Chen, W. Li, Z. Ao, Y. Wu, X. Guan, Single-atom Fe catalyst
629 outperforms its homogeneous counterpart for activating peroxymonosulfate to
630 achieve effective degradation of organic contaminants, *Environ. Sci. Technol.* 55
631 (2021) 7034-7043. <https://doi.org/10.1021/acs.est.0c08805>

632 [64] S. Lanzalaco, I. Sirés, M.A. Sabatino, C. Dispenza, O. Scialdone, A. Galia, Synthesis
633 of polymer nanogels by electro-Fenton process: investigation of the effect of main
634 operation parameters, *Electrochim. Acta* 246 (2017) 812-822.
635 <https://doi.org/10.1016/j.electacta.2017.06.097>

636 [65] Z. Ye, J.A. Padilla, E. Xuriguera, E. Brillas, I. Sirés, Magnetic MIL(Fe)-type MOF-
637 derived N-doped nano-ZVI@C rods as heterogeneous catalyst for the electro-Fenton
638 degradation of gemfibrozil in a complex aqueous matrix, *Appl. Catal. B: Environ.*
639 266 (2020) 118604. <https://doi.org/10.1016/j.apcatb.2020.118604>

640 [66] W. Ren, D. Tang, Lu, X. Sun, J. Li, M. Qiu, S. Fan, Novel multilayer
641 ACF@rGO@OMC cathode composite with enhanced activity for electro-Fenton
642 degradation of phthalic acid esters, *Ind. Eng. Chem. Res.* 55 (2016) 11085-11096.
643 <https://doi.org/10.1021/acs.iecr.6b02896>

644 [67] Y. Li, N. Luo, Z. Tian, H. Li, M. Yang, W. Shang, Y. Shen, M. Qu, A. Zhou, H₂O₂-
645 free photo-Fenton degradation of organic pollutants on thermally exfoliated g-C₃N₄,
646 *Colloid. Surface. A* 586 (2020) 124190.
647 <https://doi.org/10.1016/j.colsurfa.2019.124190>

648 [68] Z. Guo, Y. Xie, J. Xiao, Z. Zhao, Y. Wang, Z. Xu, Y. Zhang, L. Yin, H. Cao, J.
649 Gong, Single-atom Mn-N₄ site-catalyzed peroxone reaction for the efficient

650 production of hydroxyl radicals in an acidic solution, *J. Am. Chem. Soc.* 141 (2019)
651 12005-12010. <https://doi.org/10.1021/jacs.9b04569>
652 [69] W. Xu, W. Xue, H. Huang, J. Wang, C. Zhong, D. Mei, Morphology controlled
653 synthesis of α -Fe₂O_{3-x} with benzimidazole-modified Fe-MOFs for enhanced photo-
654 Fenton-like catalysis, *Appl. Catal. B: Environ.* 291 (2021) 120129.
655 <https://doi.org/10.1016/j.apcatb.2021.120129>

1 **Figure captions**

2 **Fig. 1.** (a) Scheme of the preparation method of the Fe-SAC/NC, ending in a
3 representation of the atomic network. (b-d) TEM images of the obtained Fe-SAC/NC, at
4 different magnifications.

5 **Fig. 2.** XRD patterns of (a) Fe-SAC/NC and ZIF-8-derived NC and (b) Fe-NP/NC. High
6 resolution (c) Fe 2*p* and (d) N 1*s* XPS spectra of Fe-NP/NC (prepared with 0 g CTAB)
7 and Fe-SAC/NC (prepared with 1.0 g CTAB). (e) The pyrrolic N and Fe-N percentages
8 in the catalysts with the CTAB content employed during the synthesis. (f) Raman spectra
9 of Fe1/2Zn-1.0CTAB and Fe1/2Zn-1.5CTAB.

10 **Fig. 3.** (a) XANES curves and (b) FT-EXAFS curves at Fe K-edge obtained for Fe foil,
11 FeO, Fe₂O₃, and Fe-SAC/NC. (c) Corresponding fitting for the FT-EXAFS curve of Fe-
12 SAC/NC over the R space range (inset: model of FeN₄ site in Fe-SAC/NC; the red, pink,
13 and blue balls represent Fe, N and C, respectively). (d) Wavelet transform (WT) contour
14 plots of Fe K-edge for Fe foil, FeO, Fe₂O₃ and Fe-SAC/NC.

15 **Fig. 4.** (a) Normalized 2,4-DCP concentration decay during different treatments of 160
16 mL of 0.14 mM 2,4-DCP solutions with 0.05 M Na₂SO₄. (b) Effect of CTAB dosage,
17 employed during the catalyst preparation, on the catalytic performance during the HEF
18 treatment of 2,4-DCP solutions (inset: the corresponding kinetic analysis and pseudo-
19 first-order rate constants). (c) Dependence of the rate constant values (*k*_{obs}) for 2,4-DCP
20 degradation (extracted from [Fig. 4b](#)). Effect of (d) catalyst dosage and (e) initial pH on
21 the time course of normalized 2,4-DCP concentration during the Fe-SAC/NC-catalyzed
22 HEF treatment (inset in (d): iron concentration after 90 min treatment). (f) Iron
23 concentration and final pH after 90 min of the electrolytic trials shown in [Fig. 4e](#).

24

25 **Fig. 5.** (a) The degradation performance of Fe-SAC/NC-catalyzed HEF process
26 considering different target organic pollutants, e.g., naproxen (NPX), 2,4-DCP,
27 trimethylolpropane (TMP), ciprofloxacin (CIP), Methyl Orange (MO), and Rhodamine
28 B (RhB). (b) Recycling of Fe-SAC/NC in the HEF treatment of 2,4-DCP solutions.
29 (Unless otherwise stated, the parameters in each figure are: TOC of 10 mg L⁻¹ C;
30 [Catalyst] = 0.10 g L⁻¹; initial pH = 4.0; applied current = 50 mA). (c) Degradation of 2,4-
31 DCP in 160 mL of urban wastewater by Fe-SAC/NC-catalyzed HEF process at pH 4.0
32 and applied current of 50 mA. (d) Change of normalized TOC with reaction time during
33 HEF treatment of 2,4-DCP solutions using a DSA or BDD anode under the conditions of
34 the trial shown in [Fig. 4a](#).

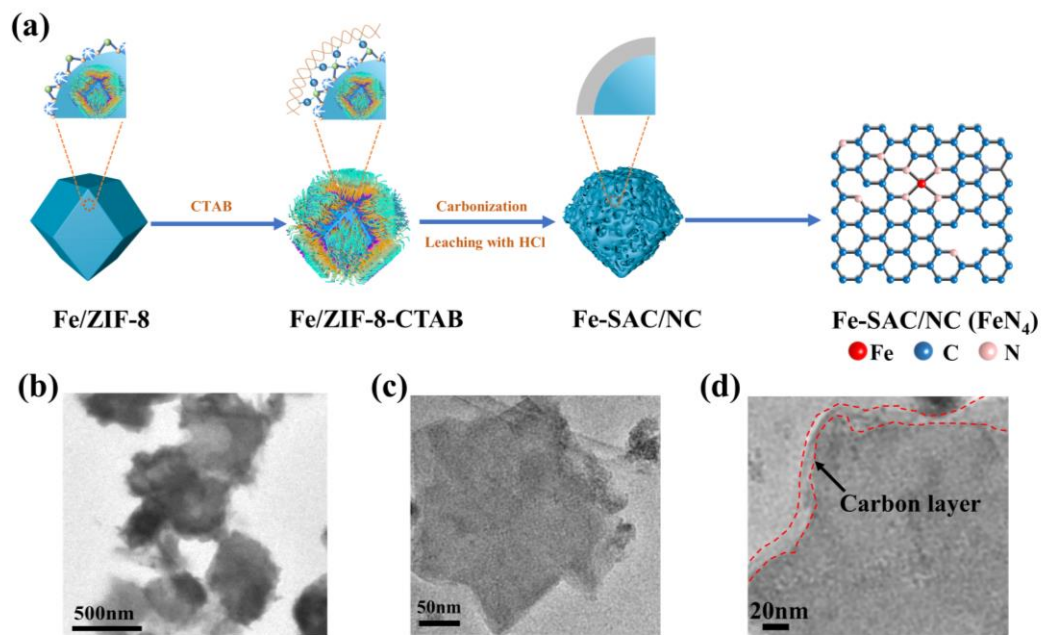
35 **Fig. 6.** Reaction pathways for H₂O₂ adsorption and activation at FeN₄ and Fe₃N sites, and
36 required energy calculated by DFT.

37 **Fig. 7.** Proposed mechanism for Fe-SAC/NC-catalyzed HEF degradation of 2,4-DCP.

38

39

40



41

42

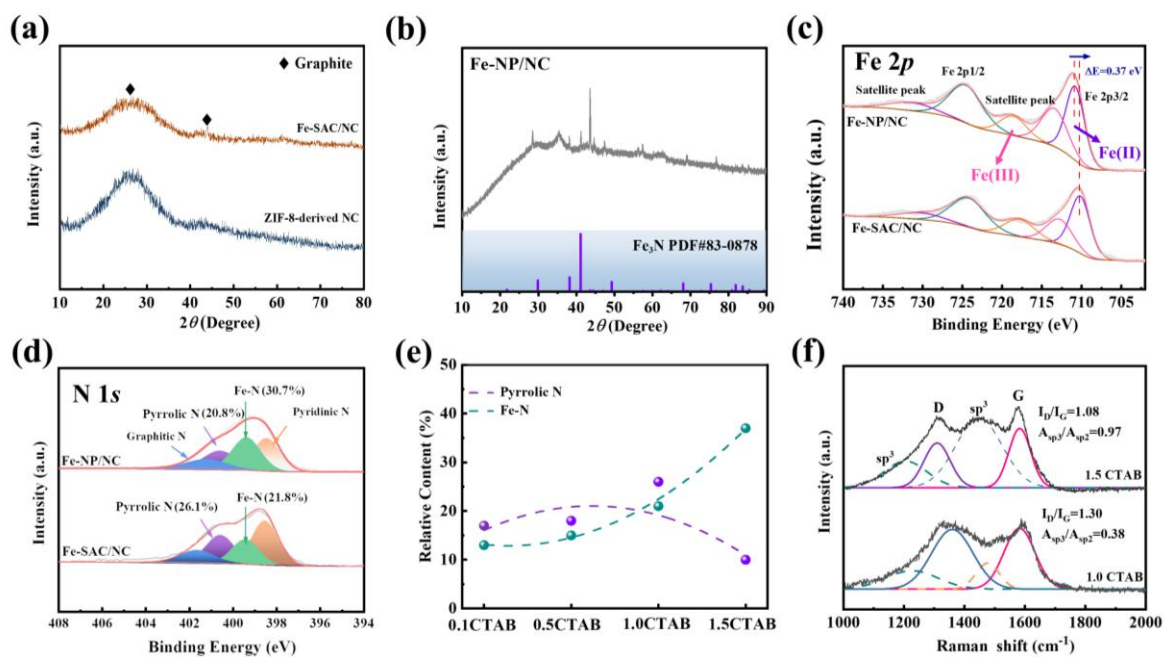
43

Fig. 1

44

45

46



47

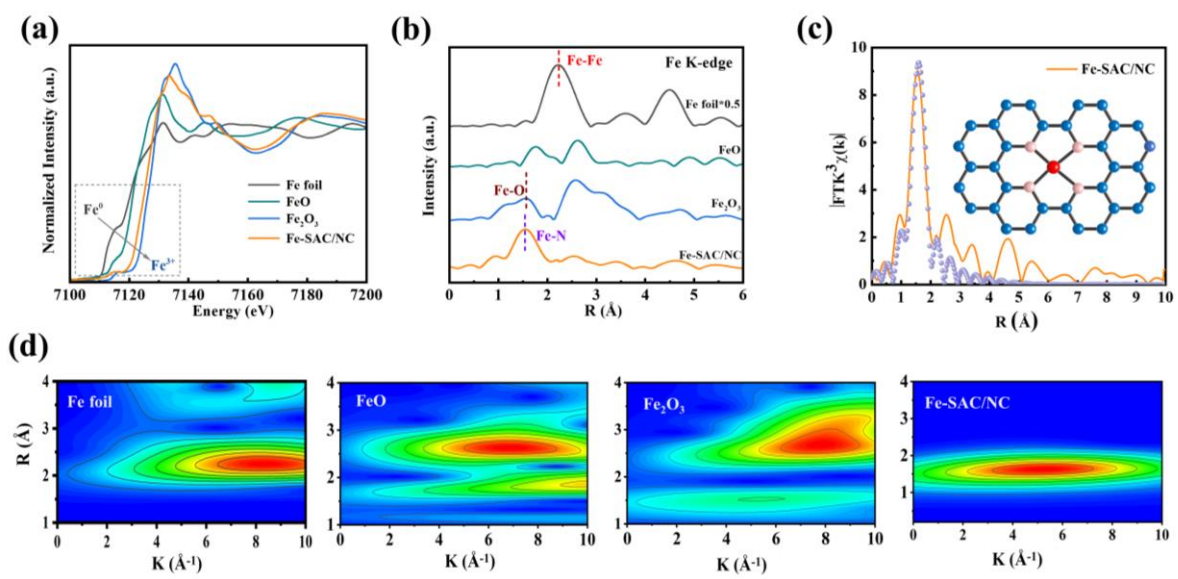
48

Fig. 2

49

50

51



52

53

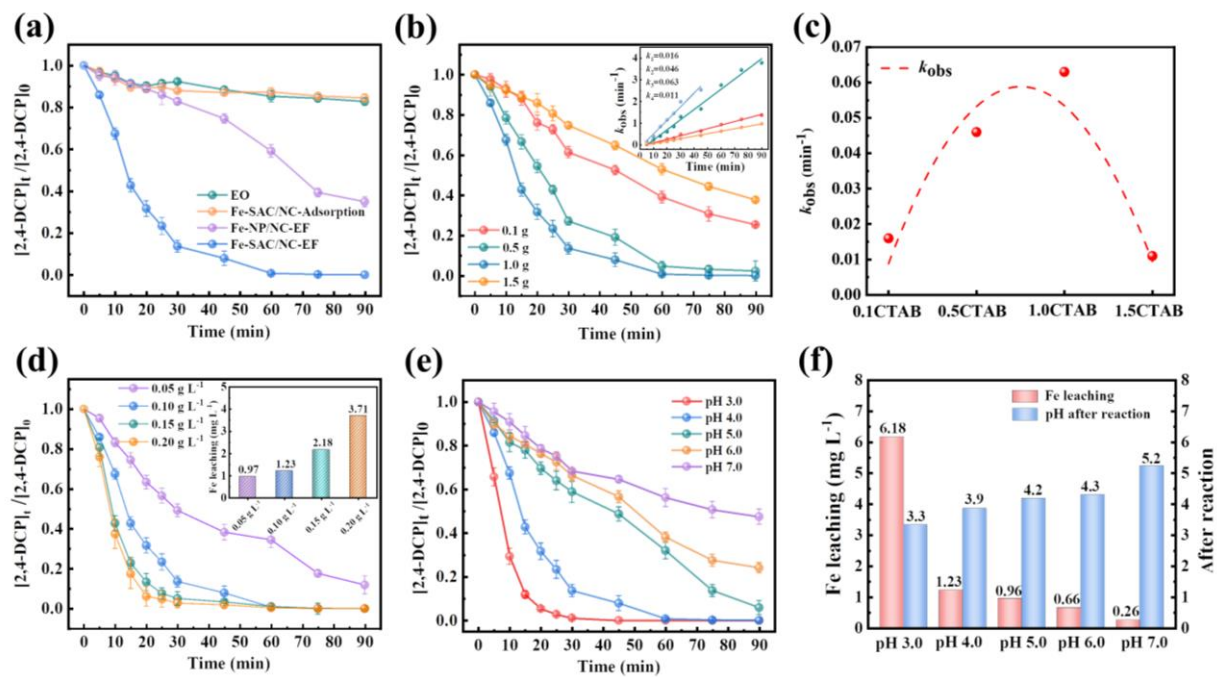
Fig. 3

54

55

56

57



58

59

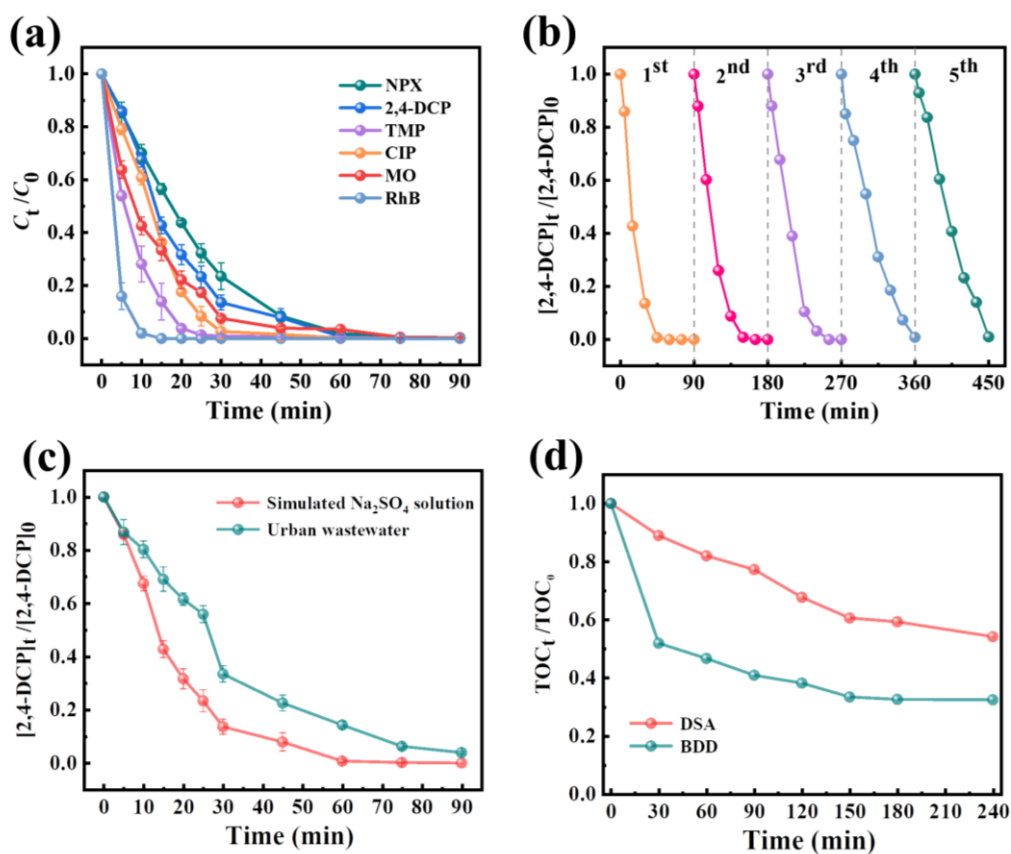
60

Fig. 4

61

62

63



64

65

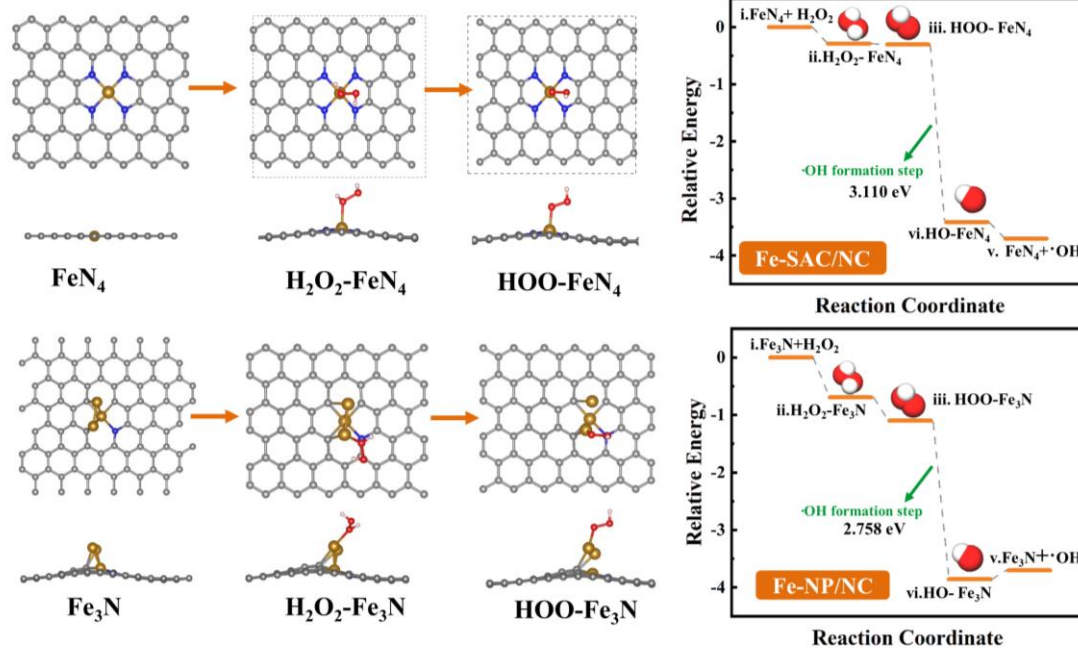
Fig. 5

66

67

68

69



70

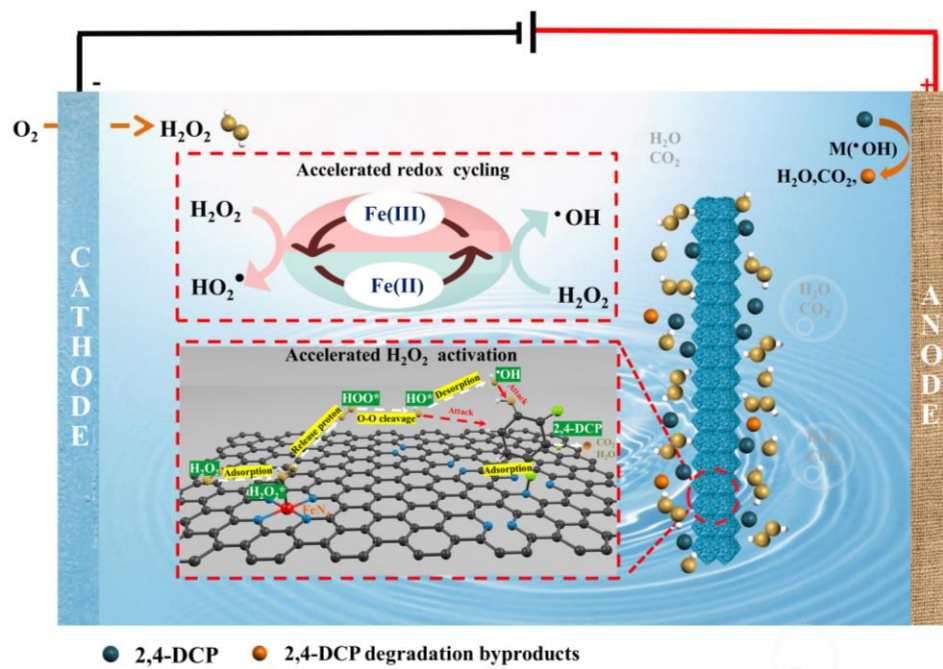
71

Fig. 6

72

73

74



75

76

Fig. 7